Reprinted from *Analysis Methods for Multi-Spacecraft Data*
Götz Paschmann and Patrick W. Daly (Eds.),
ISSI Scientific Report SR-001 (Electronic edition 1.1)

— 7 —

Multi-Spacecraft Analysis of Plasma Kinetics

STEVEN J. SCHWARTZ
Queen Mary and Westfield College
London, United Kingdom

PATRICK W. DALY
Max Planck Institut für Aeronomie
Katlenburg-Lindau, Germany

ANDREW N. FAZAKERLEY
Mullard Space Science Laboratory
Holmbury St. Mary, United Kingdom

7.1 Introduction

Handling data from charged particle analysers which measure phase space density requires some care and attention. Even with a single satellite, the errors and uncertainties introduced by energy level and response calibrations, incomplete sampling of phase space, and discrete integration down to plasma moments (density, velocity, pressure, etc.) results in basic errors typically larger than those in, say, magnetic field measurements (see Chapter 6 for more details concerning the computation of parameters from particle instruments). Additionally, the time required to complete a sampling interval is often seconds or more, comparable to many scales of interest and intrinsic variability, so that some time aliasing is often present. Multi-spacecraft comparisons compound these difficulties. Thus many of the methods (filtering, spatial gradient and other vector operators) introduced earlier with electromagnetic fields as examples are much more difficult to apply to particle data.

On the other hand, particle data holds a richness in phase space information which can be exploited to reveal the physical processes which govern the dynamics, and which can probe/remote sense non-local structures. Nearly all such work is based on applications of Liouville's Theorem. In this chapter we explore some of the ways in which this phase space information can be utilised. One major difference between these multi-spacecraft particle techniques and those discussed earlier with respect to lower dimensional, higher time resolution field data is that very often the particle techniques need to be adapted and/or designed with a single specific study in mind. Thus the techniques described below should be regarded as examples rather than off-the-shelf techniques.

Additionally, multi-species measurements provide another dimension which can be utilised. At its most basic level, measurements of both ions and electrons enables a direct measurement of the charge and current densities. Comparison of ions with different masses (or charge-to-mass ratios) probes different scalelengths and differentiates the relative contributions of different forces.

This chapter is organised as follows. In the next section, we review Liouville's Theorem, and other background information. This is followed by a discussion of techniques relating to basic moments of the particle distribution. Later sections cover various applications of Liouville's Theorem and related phase space aspects.

7.2 Liouville's Theorem

The Boltzmann equation describes the evolution of the single particle phase space distribution function $f(\boldsymbol{r}, \boldsymbol{v}, t)$:

$$\frac{\partial f}{\partial t} + \frac{\partial}{\partial \boldsymbol{r}} \cdot (\boldsymbol{v} f) + \frac{\partial}{\partial \boldsymbol{v}} \cdot (\boldsymbol{a} f) = \left(\frac{\partial f}{\partial t}\right)_{\text{collisions}} \tag{7.1}$$

where $\boldsymbol{a} = \boldsymbol{F}/m$ is the acceleration of a non-relativistic particle ($\boldsymbol{F}$ is the force) and the right-hand side includes the effects of collisions or other processes which give rise to instantaneous changes in particle velocity or position (e.g., due to creation by ionisation, etc.). The Boltzmann equation is a statement about particle conservation, and is most easily interpreted by considering the flow into and out of a fixed volume of $(\boldsymbol{r}, \boldsymbol{v})$ phase space. [For relativistic particles f is written as a function of momentum $\boldsymbol{p}$ instead of velocity. The third term in equation 7.1 becomes $\partial/\partial \boldsymbol{p} \cdot (\boldsymbol{F} f)$.]

The variables $\boldsymbol{r}$ and $\boldsymbol{v}$ are independent, so the $\boldsymbol{v}$ can be moved outside of the derivative in middle term on the left-hand side. Additionally, if the velocity divergence of the acceleration is zero, the third term can be similarly rearranged. This is the case for the Lorentz force $q(\boldsymbol{E} + \boldsymbol{v} \times \boldsymbol{B})$. If the right-hand side of the Boltzmann equation can be neglected, the result is

$$\frac{\mathrm{D}f}{\mathrm{D}t} \equiv \frac{\partial f}{\partial t} + \boldsymbol{v} \cdot \frac{\partial f}{\partial \boldsymbol{r}} + \frac{\boldsymbol{F}}{m} \cdot \frac{\partial f}{\partial \boldsymbol{v}} = 0 \tag{7.2}$$

[The relativistic form replaces $(\boldsymbol{F}/m) \cdot \partial f/\partial \boldsymbol{v}$ with $(\boldsymbol{F}) \cdot \partial f/\partial \boldsymbol{p}$.] The operator

$$\frac{\mathrm{D}}{\mathrm{D}t} \equiv \frac{\partial}{\partial t} + \boldsymbol{v} \cdot \frac{\partial}{\partial \boldsymbol{r}} + \frac{\boldsymbol{F}}{m} \cdot \frac{\partial}{\partial \boldsymbol{v}} \tag{7.3}$$

represents the Lagrangian or convective derivative following a single particle trajectory $(\boldsymbol{r}(t), \boldsymbol{v}(t))$ in phase space. Thus equation 7.2 can be interpreted as a statement that phase space density is constant along particle trajectories in phase space, i.e.,

$$f(\boldsymbol{r}, \boldsymbol{v}, t) = f(\boldsymbol{r}_o, \boldsymbol{v}_o, 0) \tag{7.4}$$

where $\boldsymbol{r}(t)$ and $\boldsymbol{v}(t)$ are solutions of the particle equations of motion

$$\begin{aligned} \frac{\mathrm{d}\boldsymbol{r}}{\mathrm{d}t} &= \boldsymbol{v} \\ \frac{\mathrm{d}\boldsymbol{v}}{\mathrm{d}t} &= \frac{\boldsymbol{F}}{m} \end{aligned} \tag{7.5}$$

[or $\mathrm{d}\boldsymbol{p}/\mathrm{d}t = \boldsymbol{F}$] with initial condition $\boldsymbol{r}(0) = \boldsymbol{r}_o$ and $\boldsymbol{v}(0) = \boldsymbol{v}_o$. This is Liouville's Theorem, which reduces the task of solving equation 7.2 to one of solving single particle motion. Liouville's Theorem provides the basic tool for analysing multi-spacecraft particle data at the level of phase space density. The theorem is a very powerful, but easily misused, approach to a variety of kinetic problems. We discuss a few typical applications below, although individual problems often require specifically tailored techniques.

Most applications of Liouville's Theorem rely on the further assumptions of adiabatic particle motion in static or slowly varying fields. Magnetic moment conservation, for example, yields

$$\frac{v_\perp^2}{B} = \frac{v_{\perp o}^2}{B_o} \tag{7.6}$$

where $v_\perp$ is the particle gyro-speed perpendicular to the magnetic field. Energy conservation in an electrostatic potential further yields

$$v_\parallel^2 + v_\perp^2 + 2q\phi/m = v_{\parallel o}^2 + v_{\perp o}^2 + 2q\phi_o/m \tag{7.7}$$

Equations 7.6 and 7.7 completely characterise the particle trajectory with these assumptions if the fields B and ϕ are given/known.

7.3 Liouville Mapping: Known Fields

If the (dc) electromagnetic fields are known, Liouville's Theorem can be used to study the extent to which scattering or other non-dc effects influence the particle response. Additionally, Liouville's Theorem provides a valuable tool for exploring boundaries in velocity space which can often be seen in particle data. These boundaries or features occur, e.g., as separators between different sources of plasmas. The shape and timing of such boundaries provides rich information about the plasma source, such as its location, extent, temporal variation, and properties of the electromagnetic fields and processes both at the source and during the subsequent particle motion to the spacecraft location.

Historically, applications of Liouville's Theorem have employed single spacecraft measurements by using measurements taken at different times, converting temporal variations to spatial gradients assuming time stationarity. Multi-spacecraft missions offer the possibility to map from one spacecraft location to another, thereby eliminating this assumption. However, since Liouville's Theorem deals with particle trajectories, the spacecraft in question must be connected by the trajectories of particles of interest. For particles with small gyroradii and large speeds, such as electrons, this requirement reduces to the spacecraft being connected by a magnetic field line. Slower particles and finite gyroradius effects complicate the matter, as trajectories which reach a particular spacecraft may diverge when traced backward in time, so that further assumptions of spatial homogeneity or symmetry may be required. Additionally, in a time-dependent situation, particles of different speeds arriving at the same time will have left and traversed the intervening fields at different times.

In the case where the fields are known and time stationary, the process is straightforward. Let us consider two spacecraft, numbered 1 and 2 and located at $\boldsymbol{r}_1$ and $\boldsymbol{r}_2$ respectively.

1. Solve equations 7.5 for $\boldsymbol{r}(t)$, $\boldsymbol{v}(t)$.

2. From these solutions, or from equations 7.6 and 7.7 if appropriate, deduce $\boldsymbol{v}_2(\boldsymbol{v}_1)$ corresponding to individual particle trajectories.

3. Given the measured distribution $f_1(\boldsymbol{v})$ construct the mapped distribution $f_2^m(\boldsymbol{v} = \boldsymbol{v}_2(\boldsymbol{v}_1)) \equiv f_1(\boldsymbol{v} = \boldsymbol{v}_1)$ as demanded by Liouville's Theorem. That is, assign to each velocity $\boldsymbol{v}_2$ the phase space density from the original distribution f_1 at the location in phase space $(\boldsymbol{r}_1, \boldsymbol{v}_1)$. If the original distribution f_1 is represented by contours in phase space, this amounts to taking points along the contour, mapping the motion of these points using the trajectory equations, and connecting them up with a contour whose height is identical to the original.

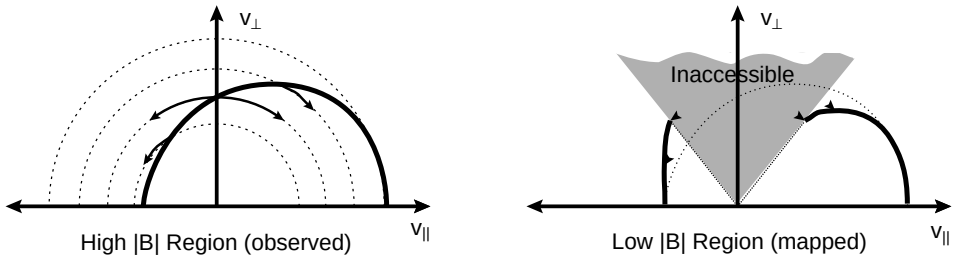

Figure 7.1: Sketch of a mapping using Liouville's Theorem to construct an expected distribution function. The solid line in the left is a contour of the observed phase space distribution in a high field region. The dotted lines are circles representing constant energy. In the absence of an electric potential, particle trajectories conserve energy and hence remain on such circles. When mapped to a low field region (assuming magnetic moment conservation), the final perpendicular velocity is given by equation 7.6. Four such trajectories are shown: two either side of 90° pitch angles, and two at intermediate pitch angles. Additionally, points at 0° and 180° pitch angles are unaltered in the mapping. The resultant mapped distribution is shown on the right (the arrowheads are left in to show the mapped points from the left diagram). Since these points started on a single contour of $f(\boldsymbol{v})$ they remain so, hence the mapped contour is found by connecting the arrowheads. Note that mapping from high to low fields, as shown here, leaves inaccessible regions in which the phase space density is filled in, if at all, by other processes or by trajectories which arrive there without passing through the high field region.

A sketch of this construction in the case of a simple magnetic field decrease and no potential difference is shown in Figure 7.1. Note that this mapping from $\boldsymbol{r}_1$ to $\boldsymbol{r}_2$ involves progressing some trajectories (e.g., $v_\parallel > 0$) forward in time while oppositely directed trajectories are advanced backward in time.

4. Compare the mapped distribution $f_2^m(\boldsymbol{v})$ with the observed one $f_2(\boldsymbol{v})$.

Discrepancies between observed and expected (mapped) distributions are indicators of one (or more) processes, e.g.,

1. Incorrect specification of the fields. This will result in systematic trends in the discrepancies in phase space. For example, an incorrect electric potential will shift all points by a fixed amount in energy.

2. Particle scattering between the two points. This will evidence itself by discrepancies localised to certain regions in phase space, with the observed distribution exhibiting generally smoother or more rounded features than the mapped ones.

3. Particle Mirroring/Inacessible Regions of Phase Space. Some regions of phase space may not be connected by trajectories which pass through both locations. For example, if a field maximum lies between the two locations, particle trajectories around 90° will mirror and never reach the second location. The mapped distribution should

therefore have holes, although the size and shape of such holes depends on knowledge of the intervening structure. Holes also arise even in the case of spatially monotonic fields due to the same mirroring arguments as shown in the example sketched in Figure 7.1. All of these holes are connected to locations beyond the second location, and thus require specification of the phase space density there, rather than at the first location. A corollary to this statement is that it is always safer to map from low magnetic field regions to high ones rather than *vice versa*, since trajectories move toward 90° in this case and such holes are avoided or at least minimised. Electrostatic potentials also give rise to inaccessible regions in phase space.

Signatures of this behaviour include the appearance of holes in the mapped distribution, ridges along, e.g., lines of constant pitch angle which separate the accessible regions (connected to the first location) from the inaccessible ones (connected to points beyond the second location), parallel/anti-parallel symmetries in the observed distribution caused by mirroring, and other similar features.

4. Lack of sufficient connection of trajectories between the two locations, lack of sufficient time-synchronisation between the two measured distributions or knowledge of the temporal and spatial of the behaviour of the fields during the measurement interval, or some other aspect which makes the mapping inappropriate.

7.4 Liouville Mapping: Unknown Fields

In many cases, the intervening fields are not known, and are of interest. For example, the electrostatic potential can be very difficult to measure directly in space. In these circumstances, the mapping procedure can be used to determine the net field/potential changes by inverting the procedure. That is, treat the unknown fields as free parameters and adjust them to yield the best agreement between mapped and observed distributions. This can be done either by trial and error or via a formalised approach having fit the observed distributions with suitable functional forms and applying, e.g., a least squares algorithm to determine the functional coefficients/constants which yield the best fit.

Note that this method can not determine the detailed spatial variation of the fields between the two locations, but only the net changes between the two locations. However, the spatial variations could give rise to inaccessible regions in phase space, so that the mapped distributions may not fit everywhere in phase space. These mis-matches actually provide information about the intervening fields (e.g., magnetic field maxima, electric potential barriers, or trapping regions). These possible intervening structures imply that some considerable caution is required in applying simple mapping methods. Such problems may be overcome to some extent by assumptions of stationarity, etc., which then provides a whole sequence of distributions corresponding to relative motion between the spacecraft and plasma. This sequence should map from one distribution to the next and to all others, enabling some determination of the spatial variation of the fields corresponding to the individual measured distributions. The prospect of three or more multipoint measurements would allow, in perhaps fortuitous circumstances, a hybrid approach using multiple mappings.

7.5 Remote Sensing of Boundaries and Non-Local Processes

In addition to sensing intervening field structure, kinetic features can be used to infer global or distant morphology and events. For example, particles energised in a transient event require a finite amount of time to reach their point of observation. *A priori*, neither the event location nor initiation time are known. However, slower particles from the same event take longer to travel the same distance. In its simplest form, one can write down the trajectory as

$$x_{\text{obs}} - x_{\text{event}} = v \times (t_{\text{obs}}(v) - t_{\text{event}}) \tag{7.8}$$

Thus the time history of different velocity particle arrivals can be used to solve this set of equations for the unknown event position, x_{event} and event time t_{event}. In the sections which follow, we use similar arguments applied to more complicated situations. All of them rely on Liouville's Theorem, either explicitly or (as here) implicitly.

Additionally, such information is often used qualitatively to locate the observation point with respect to remote boundaries. For example, the Earth's bow shock is a copious source of suprathermal electrons, accelerated at the shock itself or escaping in the form of a broad heat flux from the hot magnetosheath. Thus the presence of such electrons implies that the observation point lies on a magnetic field line which is connected to the bow shock. In this regard, electrons have the advantage that their gyroradii are negligible and that their speeds are higher than characteristic bulk flows, so that they essentially travel along the magnetic field lines with, to lowest order, zero time delay.

In the realm of multi-satellite observations, each satellite then measures electrons on different field lines. Treating such measurements as simple on/off indicators of connection to the bow shock, the scientist could build an image of the bow shock with as many pixels as satellites. Such an image, or sequence thereof, would provide information on the shape and dynamics of the bow shock on scales which can be much larger than the spacecraft separation depending on the geometry. The fact that field lines are neither straight nor uniform complicates this analysis, but not fatally so in all cases.

7.6 Velocity Dispersion or "Velocity Filter"

Let us consider here a localised, time-stationary source of particles, by contrast with the transient discussed in the preceding section. As an analogy, consider a pier at one side of a body of water from which boats of different speeds travel toward the opposite shore. If the supply of boats is maintained then they will all arrive at the same point at the same rate with which they left. That is to say, the distribution in phase space at the arrival point will be identical to that at the departure pier, via Liouville's Theorem.

However, if the body of water is a flowing river, the boats will suffer a convective drift in addition to their own cross-river velocity. (In the plasma case, this drift is usually the $\boldsymbol{E} \times \boldsymbol{B}$ drift.) The fastest boats will still arrive close to their previous location, but slower boats will be swept further downstream. Thus boats leaving the same point will be "dispersed" along the opposite shore according to their velocities. At a given point on the opposite shore, the convective flow has acted as a filter to allow only particles of a single velocity to pass, hence the term "velocity filter" effect, which is also in common usage,

along with "time of flight" signatures. This concept is embodied in equation 7.8 together with a y-drift equation

$$y_{\text{obs}} - y_{\text{event}} = V_{\text{drift}} \times (t_{\text{obs}}(v) - t_{\text{event}}) \tag{7.9}$$

More common, perhaps, in the magnetospheric case is not a point source, but an extended one. Consider, then, the case of a semi-infinite line of piers extending downstream from the single pier invoked above, as sketched in Figure 7.2. If one approaches from the upstream direction on the opposite bank, the first boats to be seen will be the fastest ones which departed from the end pier. Downstream of this point, slightly slower boats from the end pier will arrive together with the fastest boats from the second pier. As one progresses further downstream, the fastest boats are always present and the distribution of arriving boats extends progressively to lower speeds as shown in the Figure.

This is what happens at the Earth's bow shock, or for that matter any shock of finite extent, such as slow mode reconnection shocks in the geomagnetic tail, and is known as the "foreshock" region. Well upstream of the shock, the observer is disconnected magnetically and sees no shock-related particles. Just downstream of the tangent field line (in the case of curved shocks such as the bow shock) or separatrix (in the case of reconnection shocks) the fastest particles, typically energetic electrons, will be found. As one moves deeper into the foreshock, the electron distribution fills in to lower velocities down to some "cutoff" velocity. This cutoff velocity can be related, via the simple kinematics described above, to the geometry of the situation, to the extent that foreshock "coordinates" have been devised based on distance from the tangent point of contact (or "X-point") along the magnetic field line to a point exactly upstream of the observer and a second distance from that upstream point to the observer. Deeper still lies an ion foreshock to which the same considerations, ignoring local acceleration processes, may be made. Similar reasoning has also been applied to the entry of particles into the cusp region and near the separatrix emanating from the X-line on the dayside magnetopause.

These ideas can be applied to a subset of the particle distribution (e.g., the field-aligned particles only) or to higher dimensional velocity space distributions, where magnetic moment conservation, or other trajectory considerations, must be included.

To date, the vast majority of applications have relied on data from a single spacecraft. Multiple spacecraft can be used as a collection of single spacecraft, to effectively determine the geometry of a physical region. Additionally, well-placed spacecraft can be used to apply some of the Liouville mapping techniques described above to map from source region to distant observation point, thereby shedding light on the intervening local processes which shape the distribution or provide local acceleration or scattering. Moreover, multiple spacecraft enable one to distinguish a localised source which is switched on at some time from a more extended source with a foreshock, as entering a foreshock yields a spacecraft time sequence which is very similar to that for a temporal switch on.

7.7 Particle Anisotropies and Remote Sensing

7.7.1 The Gyro-Orbit

Charged particles in a magnetic field describe a circular orbit perpendicular to the magnetic field vector $\boldsymbol{B}$, together with a motion parallel to the field producing a spiral

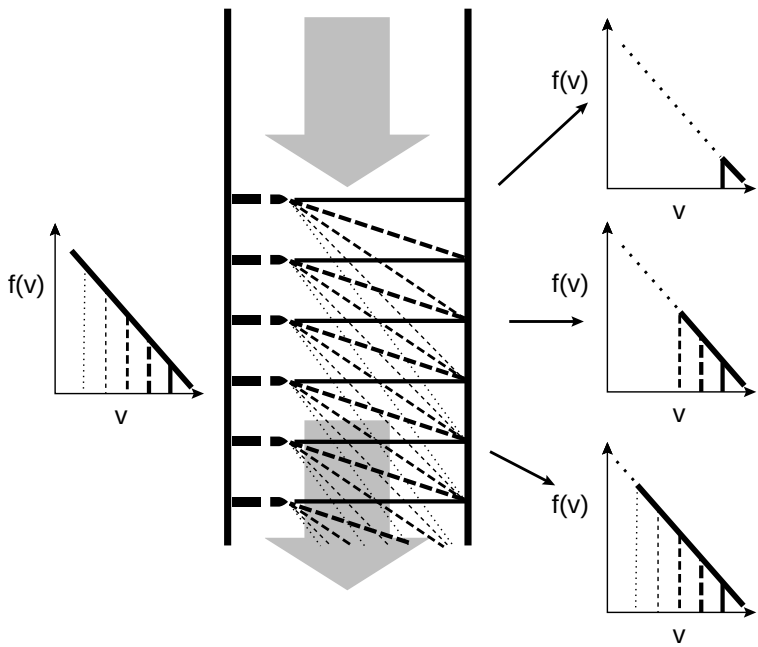

Figure 7.2: Velocity dispersion due to convective drift. A semi-infinite set of piers on the left all launch a range of boats whose velocity distribution function is shown to the left. The fastest boats (thick solid lines) travel in nearly horizontal lines, while slower boats (progressively thinner and more dotted lines) also suffer convection by the flow (broad grey arrows). On the opposite side of the river, the observed distribution of boats arriving depends on location. At the most upstream locations, no boats are seen. Moving downstream, first only the fastest boats are seen. Still further downstream slower boats from more upstream piers, together with faster boats from the opposite piers, are seen. Liouville's Theorem forces the phase space density to be constant along trajectories, enabling us to construct the observed distribution functions, as shown on the right for three locations. Note the cutoff at low velocities, and the way this cutoff systematically moves to lower velocities with downstream position.

trajectory. The frequency and radius of this "gyromotion" are given by

$$\omega = \frac{qB}{m} \tag{7.10}$$

$$R_g = \frac{mv_\perp}{qB} = \frac{\sqrt{2mE}}{qB}\sin\beta \tag{7.11}$$

where $v_\perp$ is the particle velocity perpendicular to the magnetic field, and β is the pitch angle between $\boldsymbol{v}$ and $\boldsymbol{B}$.

Equation 7.11 can also be written in vector form:

$$\boldsymbol{R}_g = \frac{m}{qB^2}\,\boldsymbol{v}\times\boldsymbol{B} \tag{7.12}$$

where $\boldsymbol{R}_g$ is the vector from the particle's position to its gyrocentre.

For protons, one can write

$$R_g = 4569.4\,\text{km}\cdot\frac{\sqrt{E/\text{keV}}}{B/\text{nT}}\sin\beta \tag{7.13}$$

Table 7.1 lists some sample results from equation 7.13, demonstrating that the gyroradius of energetic protons is quite comparable to the scale lengths of magnetospheric processes. For heavier ions, the gyroradius is even larger, scaling with $\sqrt{m}$ (equation 7.11). On the other hand, electrons in these energy and field ranges possess gyroradii on the order of 100 km or less, too small for any observable effects normally.

Table 7.1: Sample proton gyroradii and periods

	10 nT	100 nT
10 keV	1400 km	140 km
100 keV	4600 km	460 km
Period	6.5 s	0.65 s

7.7.2 Particle Anisotropies

One of the most straightforward particle observations is a measure of the particle anisotropies, that is, the extent to which the distribution function deviates from isotropy in velocity space. Anisotropies can arise due to the relative motion of the observer with respect to the frame associated with an isotropic particle source, due to gradients in the intervening medium, or to additional sources, sinks, or scattering of the particles en route to the observer. First order directional anisotropies are most easily interpreted as net particle streaming. Here we outline the basic calculation of the expected anisotropies due to two effects: a gradient in the particle density and intrinsic first order anisotropies due to either constant velocity shifts (same for all particles) or more complex distributions. The

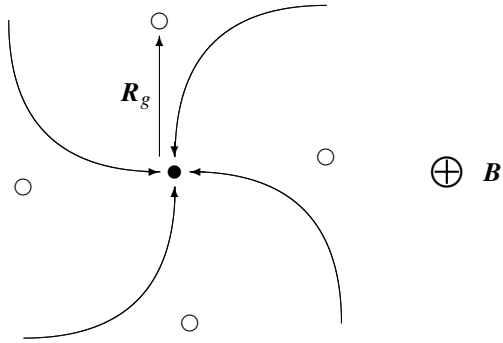

Figure 7.3: Ions impinging an observation point (black dot) from several directions; the gyrocentres of each orbit (open circles) are displaced by $\boldsymbol{R}_g$; the magnetic field $\boldsymbol{B}$ points into the paper.

first is related to the finite extent of the particle gyro-orbit and to spatial inhomogeneities. The second is purely a velocity-space property. If the mechanism(s) responsible for the anisotropy are known, a measurement of the local particle anisotropy provides direct inference of non-local characteristics (density gradients, source region velocity, etc.). We return later to the question of which effects are likely to be observable, as often there are competing processes which give rise to a reduced level of anisotropy.

The starting point for all such calculations is the basic conservation of particles. Let us assume that there is a spatial gradient in the number of particles. Due to the rapid gyromotion, the assumed spatial gradient will refer to particles' gyrocentre (or "guiding centre") as in Figure 7.3. Additionally, we assume that the particles' velocity distribution takes on a relatively simple, known form in a frame of reference moving with a bulk velocity $\boldsymbol{V}$ with respect to the spacecraft frame.

Thus the problem commences by relating the phase space density $f(\boldsymbol{r}, \boldsymbol{v})$ in the spacecraft frame to the spatially-dependent, velocity distribution $f_{GC}(\boldsymbol{r}_{GC}, \boldsymbol{v}')$. The vector $\boldsymbol{r}_{GC}$ is the position of the guiding centre of a particle whose instantaneous position and velocity are $\boldsymbol{r}$ and $\boldsymbol{v}$. The velocity in the moving frame is denoted $\boldsymbol{v}'$. In practice, the spatial dependence of f_{GC} may be linked to the spatial dependencies of other parameters, such as B, which we shall ignore here. Equating the number of particles in an elemental volume in each coordinate system gives

$$f(\boldsymbol{r}, \boldsymbol{v})\ \mathrm{d}^3r\ \mathrm{d}^3v = f_{GC}(\boldsymbol{r}_{GC}, \boldsymbol{v}')\ \mathrm{d}^3r_{GC}\ \mathrm{d}^3v' \tag{7.14}$$

This deceptively simple statement reduces the entire problem, and many similar to it, to one of coordinate transformation. In this case, the transformation laws are given by

$$\boldsymbol{r}_{GC} = \boldsymbol{r} + \boldsymbol{R}_g \tag{7.15}$$

$$\boldsymbol{v}' = \boldsymbol{v} - \boldsymbol{V} \tag{7.16}$$

Using equation 7.12 and assuming $\boldsymbol{B}$ is uniform, it is straightforward to show that the jacobian relating $\mathrm{d}^3r\ \mathrm{d}^3v$ and $\mathrm{d}^3r_{GC}\ \mathrm{d}^3v'$ is unity in this case. It therefore follows from equation 7.14 that

$$f(\boldsymbol{r}, \boldsymbol{v}) = f_{GC}(\boldsymbol{r}_{GC}, \boldsymbol{v}') \tag{7.17}$$

Note that even if $f_{GC}(\boldsymbol{v}')$ is independent of gyrophase, $f(\boldsymbol{r},\boldsymbol{v})$ contains a gyrophase dependence through the $\boldsymbol{R}_g$ dependence of $\boldsymbol{r}_{GC}$.

We now Taylor expand the right-hand side of equation 7.17 about the point in phase space ($\boldsymbol{r}_{GC}=\boldsymbol{r}$, $\boldsymbol{v}'=\boldsymbol{v}$). This results in

$$\begin{aligned} f(\boldsymbol{r},\boldsymbol{v}) &= f_{GC}(\boldsymbol{r},\boldsymbol{v}) - \boldsymbol{V}\cdot\frac{\partial}{\partial\boldsymbol{v}}f_{GC}(\boldsymbol{r},\boldsymbol{v}) + \boldsymbol{R}_g\cdot\nabla f_{GC}(\boldsymbol{r},\boldsymbol{v}) \\ &\quad + \mathcal{O}\left[\left(\frac{R_g}{L}\right)^2, \frac{R_g}{L}\frac{V}{v}, \left(\frac{V}{v}\right)^2\right] \end{aligned} \tag{7.18}$$

where L is the scale length of the spatial variation of f_{GC}. Now expand the velocity dependence of $f_{GC}(\boldsymbol{r},\boldsymbol{v})$ in spherical harmonics, i.e.,

$$f_{GC}(\boldsymbol{r},\boldsymbol{v}) = f_o(\boldsymbol{r},v)\left[1+\hat{\boldsymbol{v}}\cdot\boldsymbol{\varepsilon}_o+\hat{\boldsymbol{v}}^T\mathsf{S}\,\hat{\boldsymbol{v}}+\ldots\right] \tag{7.19}$$

where $\boldsymbol{\varepsilon}_o$ is the first order anisotropy (i.e., the first degree term in the spherical harmonic expansion) and S is the second order anisotropy. We shall assume that $|\mathsf{S}| \ll |\boldsymbol{\varepsilon}_o| \ll 1$ and restrict our calculations to first order results. The various derivatives of $f_{GC}(\boldsymbol{r},\boldsymbol{v})$ are now easily calculated in terms of this expansion as

$$\nabla f_{GC}(\boldsymbol{r},\boldsymbol{v}) = \nabla f_o(\boldsymbol{r},v)\,[1+\mathcal{O}(\boldsymbol{\varepsilon}_o)] \tag{7.20}$$

$$\begin{aligned} \frac{\partial f_{GC}(\boldsymbol{r},\boldsymbol{v})}{\partial\boldsymbol{v}} &= \frac{\partial f_o(\boldsymbol{r},v)}{\partial\boldsymbol{v}}\,[1+\mathcal{O}(\boldsymbol{\varepsilon}_o)] \\ &= \hat{\boldsymbol{v}}\frac{\partial f_o(\boldsymbol{r},v)}{\partial v}\,[1+\mathcal{O}(\boldsymbol{\varepsilon}_o)] \end{aligned} \tag{7.21}$$

Substituting the results from equations 7.19–7.21 into equation 7.18 brings us finally to ⇒7.1

$$\begin{aligned} f(\boldsymbol{r},\boldsymbol{v}) &= f_o(\boldsymbol{r},v)\Bigg[1+\hat{\boldsymbol{v}}\cdot\boldsymbol{\varepsilon}_o+\boldsymbol{R}_g\cdot\nabla\ln f_o(\boldsymbol{r},v)-\boldsymbol{V}\cdot\hat{\boldsymbol{v}}\frac{\partial\ln f_o(\boldsymbol{r},v)}{\partial v} \\ &\quad + \mathcal{O}\left(S, \frac{R_g}{L}\varepsilon_o, \frac{V}{v}\varepsilon_o, \left(\frac{R_g}{L}\varepsilon_o\right)^2, \frac{R_g}{L}\frac{V}{v}, \left(\frac{V}{v}\right)^2\right)\Bigg] \end{aligned} \tag{7.22}$$

Using equation 7.12 for $\boldsymbol{R}_g$, swapping dot and cross product, and general tidying leads to

$$f(\boldsymbol{r},\boldsymbol{v}) \approx f_o(\boldsymbol{r},v)\left[1+\hat{\boldsymbol{v}}\cdot\boldsymbol{\varepsilon}_o+\hat{\boldsymbol{v}}\cdot\boldsymbol{\varepsilon}_{C-G}+\hat{\boldsymbol{v}}\cdot\boldsymbol{\varepsilon}_{\nabla n}\right] \tag{7.23}$$

where

$$\boldsymbol{\varepsilon}_{C-G} \equiv -\frac{\boldsymbol{V}}{v}\frac{\partial\ln f_o}{\partial\ln v} \tag{7.24}$$

is the Compton-Getting anisotropy and

$$\boldsymbol{\varepsilon}_{\nabla n} \equiv \frac{mv}{qB^2}\boldsymbol{B}\times\nabla\ln f_o \tag{7.25}$$

is the density gradient-induced anisotropy.

The above forms are not the way these anisotropies are usually presented, because the energetic particle detectors on which most observations are based do not measure f directly. The detector count rate N_{ijk}/t_{acc} is proportional to the differential intensity, $\mathrm{d}J/\mathrm{d}E$,

which is the number of particles per unit area per second per steradian per unit energy (E) travelling in the direction $\hat{\boldsymbol{v}}$ (see Chapter 5, particularly Section 5.2.3). Relating $\mathrm{d}J/\mathrm{d}E$ to f is easily accomplished by returning to an expression for the number of particles in an elemental phase space volume, which in this case becomes

$$f(\boldsymbol{r}, \boldsymbol{v})\ \mathrm{d}^3r\ \mathrm{d}^3v = \frac{\mathrm{d}J}{\mathrm{d}E}\ \mathrm{d}A\ \mathrm{d}t\ \mathrm{d}\Omega\ \mathrm{d}E \tag{7.26}$$

Noting $\mathrm{d}A\ v\mathrm{d}t = \mathrm{d}^3r$, $\mathrm{d}E = mv\ \mathrm{d}v$ (for non-relativistic particles), and $\mathrm{d}^3v = v^2\ \mathrm{d}v\ \mathrm{d}\Omega$ leads to the conclusion that f and $\mathrm{d}J/\mathrm{d}E$ are related by

$$\frac{v^2}{m} f(\boldsymbol{r}, \boldsymbol{v}) = \frac{2E}{m^2} f(\boldsymbol{r}, \boldsymbol{v}) = \frac{\mathrm{d}J}{\mathrm{d}E} \tag{7.27}$$

Thus the expansion to first order anisotropies for $\mathrm{d}J/\mathrm{d}E$ is just that obtained by multiplying equation 7.23 by the (isotropic) factor v^2/m. In particular, all the first-order Compton-Getting and density gradient anisotropies $\boldsymbol{\varepsilon}_{C-G}$ and $\boldsymbol{\varepsilon}_{\nabla n}$ are unchanged. However, we need to express them in terms of the measured parameter $\mathrm{d}J/\mathrm{d}E$. The spatial variation is simply $\nabla \ln f_o = \nabla \ln(\mathrm{d}J/\mathrm{d}E)$. Typically, $\mathrm{d}J/\mathrm{d}E$ is represented by a power law in energy of the form

$$\frac{\mathrm{d}J}{\mathrm{d}E} \propto E^{-\gamma}$$

For such a form and non-relativistic particle speeds

$$\frac{\partial \ln f_o}{\partial \ln v} = \frac{v}{f}\left[-\frac{2m}{v^3}\frac{\mathrm{d}J}{\mathrm{d}E} + \frac{m}{v^2}\frac{\mathrm{d}E}{\mathrm{d}v}\left(\frac{-\gamma}{E}\right)\frac{\mathrm{d}J}{\mathrm{d}E}\right] = -2(\gamma+1) \tag{7.28}$$

so that

$$\boldsymbol{\varepsilon}_{C-G} = 2(\gamma+1)\frac{\boldsymbol{V}}{v} \tag{7.29}$$

$$\boldsymbol{\varepsilon}_{\nabla n} = \frac{mv}{qB^2}\,\boldsymbol{B} \times \nabla \ln\left(\frac{\mathrm{d}J}{\mathrm{d}E}\right) \tag{7.30}$$

The Compton-Getting anisotropy arises because particles of fixed energy in the spacecraft frame correspond to different energies in the moving frame, depending on their direction. So although the distribution in the moving frame may be isotropic, different parts of the spectrum are being sampled at a single acceptance energy (spacecraft frame) and only the direction in the spacecraft frame is scanned. The resulting anisotropy reflects the spectral shape in the frame of bulk flow: if the spectrum were completely flat ($\partial f_o/\partial v = 0$) we have $\gamma = -1$ and $\boldsymbol{\varepsilon}_{C-G} = 0$; whereas if the slope of the spectrum goes positive, the anisotropy becomes negative, meaning it is opposite to the bulk flow $\boldsymbol{V}$. Normally the slope is negative and $\boldsymbol{\varepsilon}_{C-G} \parallel \boldsymbol{V}$. Note that particles with $v \lesssim |\boldsymbol{V}|$ are excluded from the present expansion. Treatment of these particles requires use of equation 7.17 without any approximations.

The intrinsic first order anisotropy represented by $\boldsymbol{\varepsilon}_o$ could also contain a component which would correspond likewise to a bulk velocity shift, and would incorporate the same Compton-Getting factor $2(\gamma+1)/v$. It is more natural to include this component in the bulk velocity $\boldsymbol{V}$ and reserve $\boldsymbol{\varepsilon}_o$ for first order anisotropies which are related to the internal structure of the velocity distribution function.

The density gradient anisotropy arises because there are more particle guiding centres (for a given energy) on one side than the other. For example, if there are more particles with guiding centres above the observation point shown in Figure 7.3 than below, there will be a greater flux of particles arriving from the left than from the right at the observation point; hence the observer will record an anisotropy. The anisotropy is perpendicular to both the density gradient and the magnetic field.

7.7.3 When is an Anisotropy not an Anisotropy?

The derivation given in the preceding section assumed that the only effects present were a frame transformation (and/or intrinsic first order anisotropy) and a density gradient. In fact, with the exception of the Compton-Getting anisotropy, most effects are counterbalanced by others, so that, e.g., an isolated density gradient anisotropy is rarely measured.

The fundamental argument rests with Liouville's Theorem, which requires that phase space density be constant along particle trajectories. If a distribution of particles is isotropic at some location, and particle trajectories connect the phase-space regions measured by the observer with that location, then the distortions in f are restricted to those implied by the particle trajectory solutions. A simple bulk frame shift produces the Compton-Getting effect derived above. Magnetic forces do not affect a particle's energy, and thus move particles along constant energy surfaces in velocity space which therefore cannot induce any anisotropy. And conservative electric forces act oppositely but symmetrically on trajectories coming from/going to the source location. That is, suppose particles of energy E are accelerated by such a field in coming from the source, so they appear at a higher energy $E + \Delta E$ when observed. Particles of the same observed energy $E + \Delta E$ travelling toward the source will lose an identical amount of energy, and will arrive at the source with an energy E. Since the source region corresponds, by assumption, to an isotropic velocity distribution, these two sets of particles will have the same phase-space density at the source and hence also, by Liouville's Theorem, at the observer's location. Thus the observer will also see an isotropic distribution.

Therefore, before applying the density gradient anisotropy given in Section 7.7.2 it is important to examine the process(es) which have given rise to the density gradient in the first place; such processes may themselves also lead to other anisotropies. Indeed, the above invocation of Liouville's Theorem insists that they will, and that the density gradient anisotropy will not be observed at all.

While this is a valuable lesson in the power of applying Liouville's Theorem, its naïve interpretation would suggest that first order anisotropies should be rarely observed and limited to the Compton-Getting values. In fact, first order anisotropies are frequently observed, and the reason is related to the restrictions necessary for Liouville's Theorem to hold. Some circumstances under which Liouville's Theorem is violated include:

1. when there are sources or sinks of particles;
2. when there are collisional, dissipative, or other forces for which $(\partial/\partial \boldsymbol{v}) \cdot \boldsymbol{F} \neq 0$;
3. when boundaries lead to particle trapping or exclusion, so that only portions of the distribution can be mapped from source to the spacecraft;
4. when spatial inhomogeneities lead to velocity filtering (see Section 7.6);

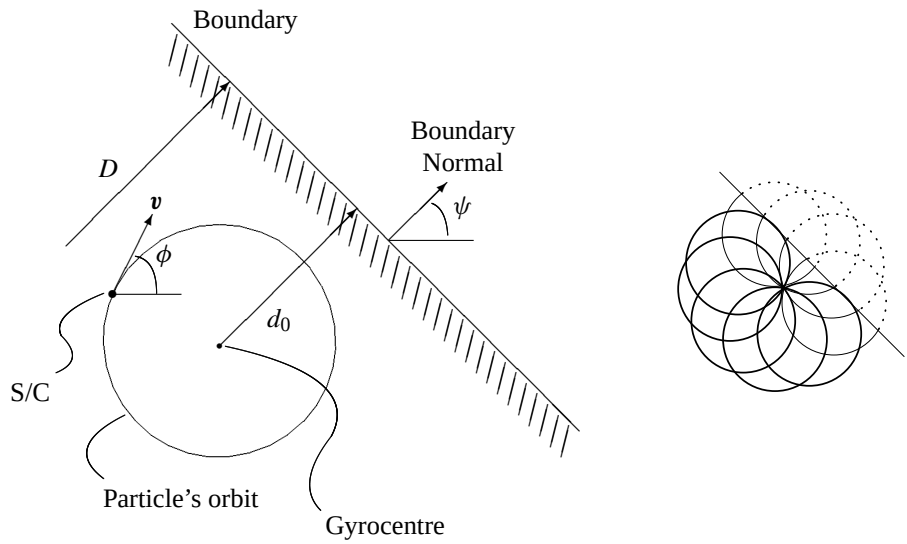

Figure 7.4: Left: the gyro-orbit of a particle whose gyrocentre is more than one gyroradius from an "absorbing" boundary. Right: snapshot of the boundary position, thick circles represent ion orbits that do not cross the absorbing boundary and therefore exhibit high intensities, while thin arcs are those parts of the trajectory connecting to the boundary, and dotted arcs are non-existent trajectories on the other side of the boundary.

5. when temporal variability at the source or elsewhere similarly leads to non-simultaneous observation of oppositely-directed trajectories.

In the next sections we explore some applications of particle kinetic effects at physical boundaries corresponding to some of these circumstances. Despite the breakdown of applicability of Liouville's Theorem (or indeed because of it), it is still possible to use mapped particle trajectories in a quantitative way to infer remote plasma sources and structure.

7.7.4 Remote Sensing of Boundaries

In Section 7.7.2, we show how a large-scale density gradient can produce a first order anistropy in the ion distributions. However, if there are very sharp gradients, such as the step function types at particle boundaries, the simple anisotropy formula of equation 7.30 no longer applies; instead, we can obtain snapshots of the moving boundary.

The left side of Figure 7.4 illustrates the gyro-orbit of an ion detected on the spacecraft (S/C) while approaching an absorbing boundary. The spacecraft is a distance D from the boundary, measured parallel to its normal, which is oriented at an angle ψ to some arbitrary reference azimuth. The ion is detected at velocity $\boldsymbol{v}$, at phase angle ϕ; its gyrocentre is a distance d_0 from the boundary.

$$d_0 = D - R_g \sin(\phi - \psi) \tag{7.31}$$

High fluxes are measured only if the entire orbit is on the particle-rich side of the boundary, for once an ion crosses the boundary on any part of it orbit, it is lost. In any real situation,

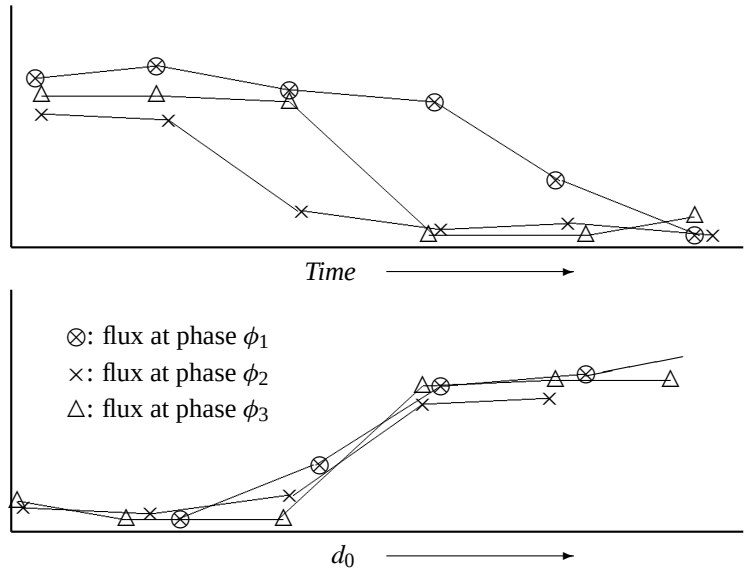

Figure 7.5: Ion fluxes plotted for 3 different phase angles as a function of time (upper) and gyrocentre distance d_0 from boundary (lower).

the boundary may also be a source of detected ions but at different flux levels related to the conditions on the other side of the boundary. For example, the magnetopause is an example of an absorbing boundary, since the magnetic field (usually) changes is configuration from one side to the other. This means that pure gyromotion cannot be maintained if an ion crosses the boundary. The ion finds itself in a field of a different orientation and adopts a new trajectory, which will not return to the spacecraft. Other ions from the far side of the boundary may cross over in such a way as to adopt a gyration that brings them to the spacecraft, giving rise to, e.g., lower flux measurements from certain arrival directions. This is illustrated in the right side of Figure 7.4, where the dotted arcs indicate non-existent particle trajectories, thin arcs indicate trajectories which take particles to or from the boundary, and thick circles indicate particle trajectories which do not intercept the boundary and so do not have reduced fluxes. As the spacecraft approaches the boundary, fluxes of particles on trajectories returning from the boundary reduce, beginning with the higher energy particles due to their larger gyroradii (see also Figure 7.6). The arrival directions at which these reduced fluxes appear span an increasing angular range as the boundary is approached. Thus, the ion flux, at a given energy and summed over all look directions, changes progressively from high to low as the spacecraft (together with the gyro-orbits arriving at the spacecraft) approaches and passes through the boundary. It is convenient to take the location of the gyrocentre itself as the indicator for high or low flux.

Displaying the boundary motion with a time series of snapshots may be very illustrative, but it would be desirable to have a more analytical method that can be reasonably automated. Particle fluxes, when plotted against time, exhibit different profiles for different phase angles, as shown in the upper plot in Figure 7.5. This "azimuthal asymmetry" results from the displacement of the various gyro-orbits. For each phase ϕ, determine the

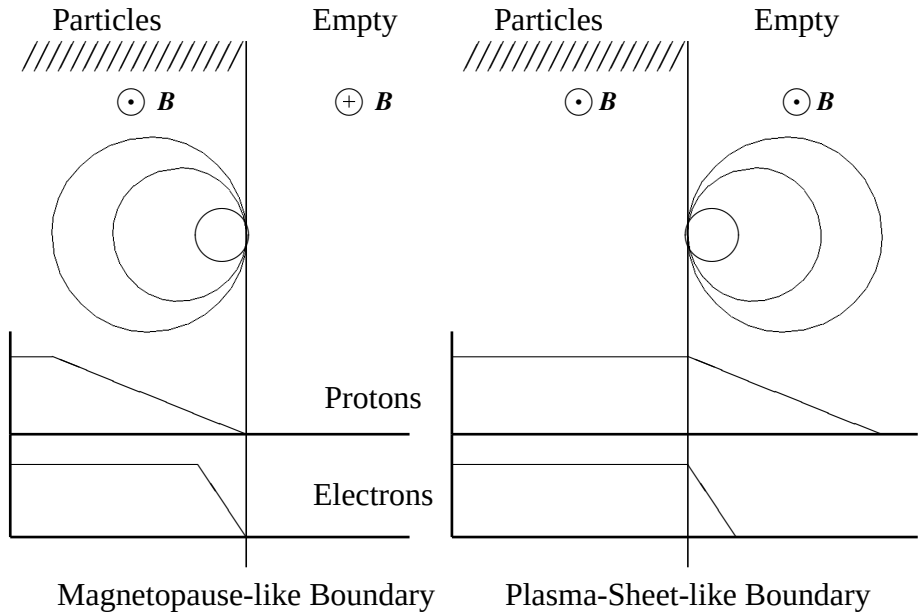

Figure 7.6: Different time profiles for flux variations while passing through a magnetopause-like, absorbing boundary (left) and a plasma-sheet-like, source boundary (right).

time $t_x(\phi)$ when its flux changes between high and low. We can now fit these switching times to a model of the boundary motion.

To do this, represent the boundary motion as $D = U(t - t_0)$; for each phase ϕ, solve equation 7.31 for the time t_x when $d_0 = 0$, the time when the gyrocentre for that phase crosses the boundary.

$$\begin{aligned} t_x(\phi) &= t_0 + \frac{R_g}{U}\sin(\phi - \psi) \\ &= t_0 + \frac{\cos\psi}{U} R_g \sin\phi - \frac{\sin\psi}{U} R_g \cos\phi \end{aligned} \tag{7.32}$$

Equation 7.32 is linear in the three unknowns t_0, $(1/U)\cos\psi$, and $(1/U)\sin\psi$. A linear least-squares fitting procedure may be applied to find these unknowns from the actual measurements of the $\{t_x(\phi)\}$.

Once the solution has been found, one can apply it to equation 7.31 to determine d_0 for each flux measurement. Plotting flux against d_0, as in the lower panel of Figure 7.5, should demonstrate that this is the parameter that best orders the high-low transitions for all phases. Furthermore, snapshots like those on the right of Figure 7.4 can be drawn with the solution for the boundary motion, as graphic evidence for its correctness.

Note: in the above example, U is negative, meaning D and d_0 decrease with time, which is why the flux increases to the right in the lower panel.

7.7.5 Absorbing or Source Boundary?

In the above example, we have demonstrated remote sensing with a boundary that empties gyro-orbits when the centres cross it, something that sounds very unphysical. After all, the ion itself is never at the gyrocentre. Instead, one can imagine two types of discontinuities that can lead to particles vanishing, shown in Figure 7.6.

Absorbing boundary where the magnetic field changes configuration, so gyro-orbits are disturbed; this type is described above. Ideally, if any part of the orbit crosses the boundary, it must be empty. The magnetopause is such a boundary. There must of course be a source of the population on the particle-rich side.

Source boundary where the magnetic field is unchanged across it, but the field line on the boundary is the last one connecting to some remote source; ions can be injected onto this last field line at such a phase that the gyrocentre is outside the source region. Thus ions can be observed up to two gyroradii beyond the boundary. This corresponds to plasma sheet boundaries, or to the division between flux transfer events and their surroundings.

As long as one restricts oneself to a single gyroradius, there is no way remote sensing can distinguish the two types: the derived boundary locations will be shifted by two gyroradii depending on the model. However, with different gyroradii, either due to other pitch angles or particle species, comparison of their behaviour could resolve this, as shown in the plots in Figure 7.6. (These are meant to be omnidirectional fluxes plotted against position.)

In reality, there may be less difference between the two models than one thinks. The absorbing boundary is not perfectly solid; the randomness of the magnetic field rotation means many ions can indeed return from a boundary crossing, or there can be those re-entering after scattering from other gyro-orbits. The source boundary too is not absolute, for those ions populating the most external gyro-orbits would be originating from only a limited range of gyrophases. When gyro-averaged, such orbits would show a reduced density.

It is therefore best to maintain the gyrocentre itself as the determining criterion for full or empty orbits, not because it is physical, but because it is an average of the fuzziness of both models. One should, however, remain aware of the true causes of the changes in flux levels at boundary crossings.

7.8 Example Applications

Numerous applications of the basic ideas presented in this chapter can be found in the literature. A small subset are shown below by way of illustration.

7.8.1 1-D Mapping of Electrons at the Earth's Bow Shock

The Earth's bow shock represents a well-studied example of a collisionless shock. The internal structure of the shock layer has received considerable attention. Thermal electrons respond adiabatically to the changes in the magnetic field and to the (field-aligned) electric field (e.g., as measured in the deHoffmann-Teller frame in which the bulk flow outside the

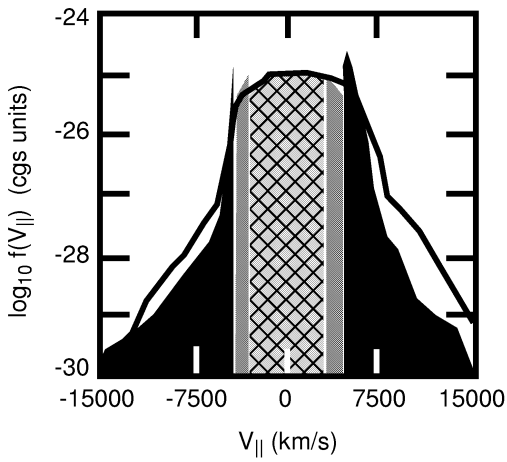

Figure 7.7: Observed (solid) and mapped (shaded) field-aligned electrons at a collisionless shock in which the fields have been determined experimentally. The innermost hatched region is inaccessible from either direction, while the intermediate region is populated by electrons originating from and returning to the downstream plasma. The outermost shaded regions correspond to electron trajectories which connect from far upstream to far downstream, and show the gross effect of the shock electrostatic field in accelerating the incident electrons to positive values (note the shifted peak). [After *Scudder et al.*, 1986, Figure 2B].

shock layer is field aligned). Figure 7.7 is taken from *Scudder et al.* [1986], and shows a cut of the electron distribution corresponding to field-aligned electrons. These electrons respond only to the electrostatic potential which, in this case, is determined observationally. The solid curve shows the measured distribution while the various shaded pieces are the result of Liouville mapping in the measured fields. The outer segments correspond to electron trajectories which connect from the asymptotic upstream to downstream states. Note the shift in the peak to positive velocities due to the acceleration by the potential. The innermost region is inaccessible from both the upstream and downstream regions (i.e., these trajectories are trapped near the vicinity of the shock), while the intervening regions correspond to electrons which start in the asymptotic downstream region, have insufficient energy to overcome the shock potential, and thus return to the downstream region. The mapping shows how well the overall features of the distribution are the result of the shock dc fields (the upstream distribution is much narrower in velocity, comparable to the width of the shifted peak).

7.8.2 2-D Electron Mapping in the Earth's Foreshock

An example of 2-D electron distributions is shown in Figure 7.8. The points represent measured electron distributions at several phase space densities taken in high field regions (top) and low field regions (bottom) within ULF waves present in the Earth's foreshock. These measured points are fit with smooth contours, in this case ellipses shown as the

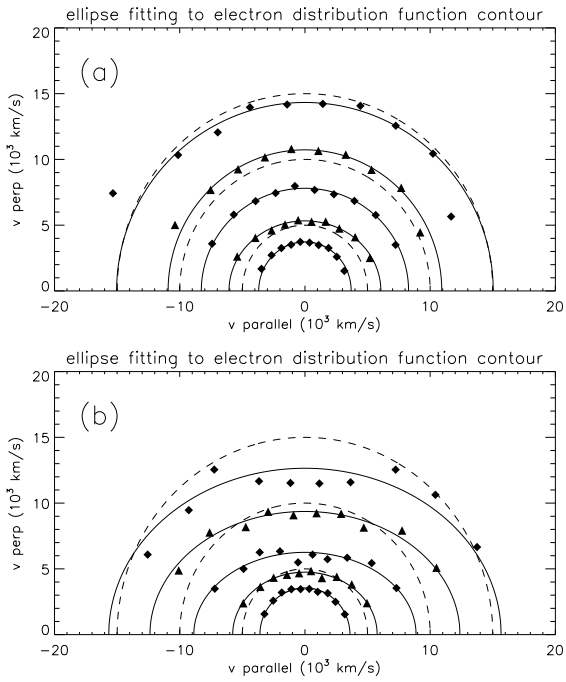

Figure 7.8: Observed contours of constant phase space density (symbols) and fitted ellipses (solid curves) in the field maxima (top) and minima (bottom) of electrons in the ULF wave field upstream of the Earth's bow shock. Dashed curves are circles to guide the eye. Adiabatic electron behaviour results in nearly isotropic contours in the high field regions, and a quantitative comparison between the fitted ellipses yields estimates of the intervening magnetic field and electric potential. [From *Chisham et al.*, 1996, Figure 6].

solid curves. Assuming adiabatic electron behaviour, equations 7.6 and 7.7 can be used to show that ellipsoidal contours map to ellipses. Moreover, if the contours at the minimum in the magnetic field are used, there are no regions inaccessible to mapped trajectories for monotonic fields and potentials (although not all trajectories starting at the minimum reach these regions). Thus the parameters of the ellipses at the same phase space density at field minimum and maximum (or anywhere in between, if desired) can be used to deduce the electrostatic field. This, together with the time variation throughout several wave cycles, is reported by *Chisham et al.* [1996]. The results show which range of electron energies (i.e., phase space densities) participate in a relatively simple adiabatic response and which regions where some other process(es) or breakdown in the assumptions occur. In principle, this method could be used when neither the electric nor magnetic field were known.

7.8.3 Remote Sensing of the Earth's Bow Shock by Field-Aligned Energetic Electrons

The Earth's bow shock is a copious emitter of suprathermal and energetic electrons into the upstream solar wind. As discussed in Section 7.6, dispersion in the foreshock re-

gion due to the velocity filter effect results in only particles above a certain (field-aligned) velocity being observed at any location behind the tangent line. The total electron population is then the superposition of the solar wind thermal population and, above this local cutoff velocity, the shock-associated energetic electrons. An example of such an electron distribution is shown in Figure 7.9. Since the cutoff velocity is related only to the geometry of the situation and the "convection" velocity, a direct measurement of this cutoff velocity and the local $\boldsymbol{E} \times \boldsymbol{B}$ convective drift enables one to reconstruct the geometry, that is, to locate the observation point in relation to the field line which is tangent to the shock. By assuming an empirical shape for the bow shock (see Section 10.4.6 on page 259), its position and scale can thus be determined. Multiple satellite studies of this kind open up the possibility to provide a more detailed, time-dependent picture of the bow shock position and shape, including local deviations from the model shape. Since these electron beams are unstable to Langmuir oscillations, direct observation of the electron beams and knowledge of the bow shock geometry provide wave analysts with an estimate of the (resonant) wave vector. This quantity can not be determined by direct wave measurements, and is crucial in theories of the nonlinear wave development.

7.8.4 Ions in the Cusp

Dayside reconnection at the magnetopause leads to an injection of energetic particles which travel along field lines and penetrate to low altitudes in the polar regions. The reconnection is associated with an $\boldsymbol{E} \times \boldsymbol{B}$ convection which results in a velocity filtering as the reconnected field lines convect poleward from the dayside. The consequence is that only ions above a cutoff energy dictated by such time-of-flight considerations will be observed at any location in the cusp. Assuming the reconnection yields a Maxwellian distribution moving along the field at the Alfvén speed in the rest frame of the field line (the deHoffmann-Teller frame), the distributions observed in the magnetosphere will be drifting Maxwellians truncated at the deHoffmann-Teller frame speed, referred to as Cowley-D distributions. An example of such a distribution is shown in Figure 7.10.

Moreover, an equatorward-moving spacecraft at low altitudes over the poles will see ions down to a cutoff velocity determined by the ion velocity and the time of flight from the reconnection site or, equivalently, distance behind the most recently reconnected field line. This is just the velocity filter effect in the curved dipole geometry of the Earth's magnetic field rather than the straight geometry depicted in Figure 7.2. An example of such a set of observations together with a sketch of the velocity filter effect in curved geometry is shown in Figure 7.11.

7.8.5 Remote Sensing of a Flux Transfer Event by Finite Gyroradius Effects

The passage of a flux transfer event (FTE) over the ISEE-2 spacecraft as observed by the medium energy particle spectrometer has been extensively analysed by *Daly and Keppler* [1983]. Figure 7.12 shows the proton intensities in various pitch angle ranges during the passage into the FTE, from low to high intensity regimes: in the left diagram, the data are plotted against time, in the right one, by the distance of the gyrocentre from the deduced boundary. This diagram is the equivalent of Figure 7.5 with real data. The FTE boundary orientation and its speed are found from the best-fit solution of equation 7.32.

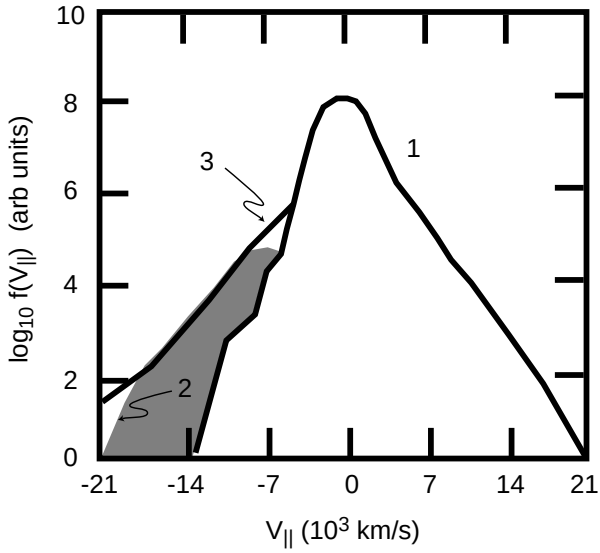

Figure 7.9: Parallel electron distributions observed with increasing penetration (1-3) into the Earth's foreshock. Note the thermal electron distribution and the superimposed electron beam (shaded) above the cutoff velocity as the foreshock is entered (2) and the extension to lower $|v_{\|}|$ in 3. [After *Feldman et al.*, 1983, Figure 1].

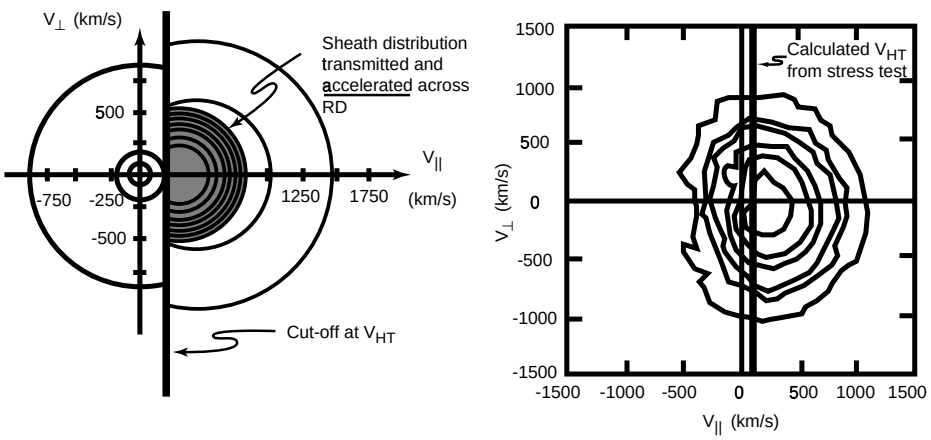

Figure 7.10: Predicted (left) and measured (right) Cowley-D distributions inside the Earth's magnetopause. The transmitted magnetosheath distributions have been accelerated by the reconnection process, and the D-shaped distribution is a consequence of the mapping and accessibility arguments discussed in this chapter. [After *Smith and Lockwood*, 1996, Figure 7].

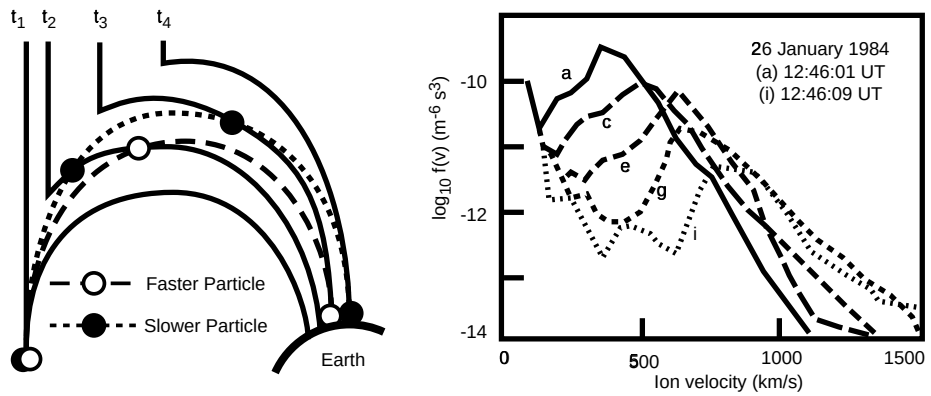

Figure 7.11: Velocity filtering in the Earth's dipole geometry (left) showing a newly reconnected field-line at successive times (solid) and the actual trajectories of particles with different speeds (dashed). Right: observations of ion distributions (right) made by a low-altitude satellite moving equatorward from (a) to (i). Note the progressive loss of lower velocity particles as the satellite moves toward the equator. Some distributions have been omitted here for clarity. [After *Onsager and Elphic*, 1996, Figure 3 (left) and *Lockwood et al.*, 1994, Figure 2 (right)].

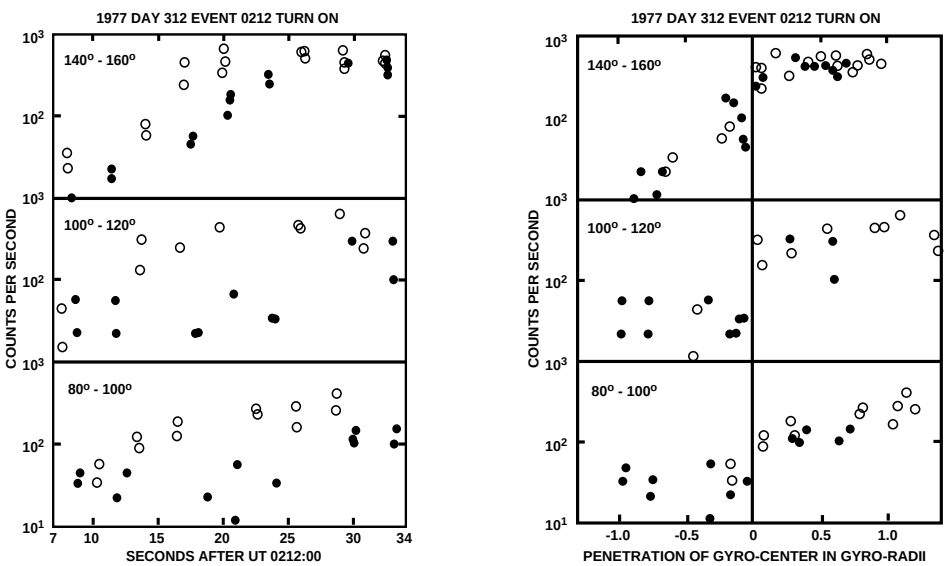

Figure 7.12: Left: plot of proton intensities against time in 3 pitch angle ranges during the entrance to the FTE; open and closed circles distinguish particles of different azimuths. Right: the same data plotted against d_0, distance of the gyrocentre inside the particle-rich side of the boundary, calculated from the best-fit solution. [From *Daly and Keppler*, 1983, Figure 4].

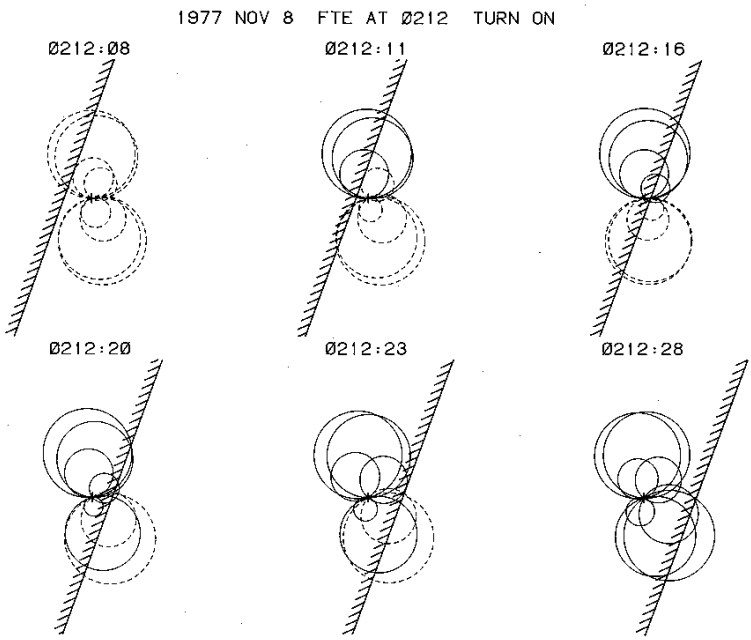

Figure 7.13: The proton gyro-orbits for 8 sectors over 6 spacecraft spins during the entrance to the FTE. The central time of each spin is printed above each plot as UT (hhmm:ss). Dashed circles are for particles of low intensities, solid ones for those of high intensity. The boundary drawn is the best-fit solution of equation 7.32. The high-intensity side of the boundary is marked by shading. [From *Daly and Keppler*, 1983, Figure 5].

The motion of the boundary is illustrated in snapshots over 6 spacecraft spins (≈4 s) in Figure 7.13, where solid and dashed circles are used to indicate gyro-orbits with high and low intensities respectively. This diagram confirms that the proton intensities switch from low to high when the gyrocentre crosses the boundary. The speed of the boundary was found to be 44 km/s along its normal, which translated into a speed for the FTE of 94 km/s, assuming it moves in the plane of the magnetopause.

Multi-spacecraft missions open up the possibility to extend such analyses from the simplifying planar assumption to more complicated boundary shapes.

Bibliography

Most basic plasma textbooks include a discussion of Liouville's Theorem. For example:

Bittencourt, J. A., *Fundamentals of Plasma Physics*, chap. 5, Pergamon Press, Oxford, 1986.

Papers that discuss Vlasov mapping at shocks are:

Scudder, J. D., Mangeney, A., Lacombe, C., Harvey, C. C., Wu, C. S., and Anderson, R. R., The resolved layer of a collisionless, high β, supercritical, quasi-perpendicular shock wave, 3. Vlasov electrodynamics, *J. Geophys. Res.*, **91**, 11 075–11 097, 1986. *The shock electron results shown in Figure 7.7 are taken from this paper.*

Schwartz, S. J., Thomsen, M. F., Feldman, W. C., and Douglas, F. T., Electron dynamics and potential jump across slow mode shocks, *J. Geophys. Res.*, **92**, 3165, 1987.

Schwartz, S. J., Thomsen, M. F., Bame, S. J., and Stansberry, J., Electron heating and the potential jump across fast mode shocks, *J. Geophys. Res.*, **93**, 12 923–12 931, 1988.

The 2-D electron mapping reproduced in Figure 7.8 is taken from:

Chisham, G., Schwartz, S. J., and Burgess, D., The anisotropy variations of electron distributions in the terrestrial ion foreshock, *J. Geophys. Res.*, **101**, 445–455, 1996.

Two-D mapping has also been invoked to explain ion behaviour in mirror mode waves in the Earth's magnetosheath, e.g.:

Leckband, J. A., Burgess, D., Pantellini, F. G. E., and Schwartz, S. J., Ion distributions associated with mirror waves in the Earth's magnetosheath, *Adv. Space Res.*, **15**, (8/9)345–(8/9)348, 1995.

Kivelson, M. G. and Southwood, D. J., Mirror instability II: The mechanism of non-linear saturation, *J. Geophys. Res.*, **101**, 17 365–17 371, 1996.

The foreshock coordinate system mentioned briefly in the text, and which has since been used by many other authors, was introduced by:

Filbert, P. C. and Kellogg, P. J., Electrostatic noise at the plasma frequency beyond the Earth's bow shock, *J. Geophys. Res.*, **84**, 1369, 1979.

The electron distribution shown in Figure 7.9 is taken from:

Feldman, W. C., Anderson, R. C., Bame, S. J., Gary, S. P., Gosling, J. T., McComas, D. J., Thomsen, M. F., Paschmann, G., and Hoppe, M. M., Electron velocity distributions near the Earth's bow shock, *J. Geophys. Res.*, **88**, 96, 1983.

The behaviour of particles in the cusp regions are reviewed by:

Smith, M. F. and Lockwood, M., Earth's magnetospheric cusps, *Rev. Geophys.*, **34**, 233–260, 1996. *Figure 7.10 is reproduced there from its original source:*

Smith, M. F. and Rodgers, D. J., Ion distributions at the dayside magnetopause, *J. Geophys. Res.*, **95**, 11 617, 1991. *This figure has been used by many authors since.*

The low-altitude satellite measurements shown at the right of Figure 7.11, together with the sketch at the left, are taken from, respectively:

Lockwood, M., Onsager, T. G., Davis, C. J., Smith, M. F., and Denig, W. F., The characteristics of the magnetopause reconnection X-line deduced from low-altitude satellite observations of cusp ions, *Geophys. Res. Lett.*, **21**, 2757–2760, 1994.

Onsager, T. G. and Elphic, R. C., Is magnetic reconnection instrinsically transient or steady-state? the Earth's magnetopause as a laboratory, *Trans. Am. Geophys. Union (EOS)*, **77**, 241–250, 1996.

Velocity filtering has been applied to good effect near the separatrices associated with the dayside X-line and in the geomagnetic tail by, respectively:

Gosling, J. T., Thomsen, M. F., Bame, S. J., Onsager, T. G., and Russell, C. T., The electron edge of the low latitude boundary layer during accelerated flow events, *Geophys. Res. Lett.*, **17**, 1833–1836, 1990.

Onsager, T. G., Thomsen, M. F., Gosling, J. T., and Bame, S. J., Electron distributions in the plasma sheet boundary layer: Time-of-flight effects, *Geophys. Res. Lett.*, **17**, 1837–1840, 1990.

Finite gyroradius effects were first intensively exploited at the magnetopause for remote sensing purposes by:

Kaufmann, R. L. and Konradi, A., Speed and thickness of the magnetopause, *J. Geophys. Res.*, **78**, 6549–6568, 1973.

Seminal work on particle anisotropies and Compton-Getting factors include:

Stern, D., The cosmic ray anisotropy, *Planet. Space Sci.*, **12**, 973–978, 1964.

Forman, M. A., The Compton-Getting effect for cosmic-ray particles and photons and the Lorentz-invariance of distribution functions, *Planet. Space Sci.*, **18**, 25–31, 1970.

See also Gleeson, L. J., The equations describing the cosmic-ray gas in the interplanetary region, *Planet. Space Sci.*, **17**, 31–47, 1969.

Example papers for the use of finite gyroradius effects to analyse the motion of a flux transfer event by the graphics method, to measure the density gradients in the plasma sheet of the geomagnetice tail, and to determine the orientation of the current sheet in the tail of comet Giacobini-Zinner, are respectively:

Daly, P. W. and Keppler, E., Remote sensing of a flux transfer event with energetic particles, *J. Geophys. Res.*, **88**, 3971–3980, 1983.

Daly, P. W., Sanderson, T. R., and Wenzel, K.-P., Survey of energetic (E>35keV) ion anisotropies in the deep geomagnetic tail, *J. Geophys. Res.*, **89**, 10 733–10 739, 1984.

Daly, P. W., Sanderson, T. R., Wenzel, K., Cowley, S. W. H., Hynds, R. J., and Smith, E. J., Gyroradius effects on the energetic ions in the tail lobes of comet P/Giacobini-Zinner, *Geophys. Res. Lett.*, **13**, 419–422, 1986

analysis of plasma kinetics, in Analysis Methods for Multi-Spacecraft. Data, edited by G. Paschmann and P. W. Daly, ISSI Sci. Rep.Â Previously, a multipoint spacecraft analysis method using Cluster data was applied to analyze only two foreshock cavitons, and this method did not consider uncertainties. In this study, multipoint spacecraft analysis methods, including the timing method, the minimum directional derivative (MDD) method, and the spatiotemporal difference (STD) method are applied to determine the velocity in both spacecraft and solar wind frames. The propagation properties show good agreement with previous results from simulations and observations that most cavitons move sunward in the solar wind frame, with the Computer Space Plasma Physics: Simulation Techniques and Soft-wares, pp. 21â€“65. Terra Scientific, Tokyo (1993)Google Scholar. 3.Â Okada M., Usui H., Omura Y., Ueda H.O., Murata T., Sugiyama T. (2008) Spacecraft Plasma Environment Analysis Via Large Scale 3D Plasma Particle Simulation. In: Labarta J., Joe K., Sato T. (eds) High-Performance Computing. ISHPC 2005, ALPS 2006.